

Multiple magnetic transitions and complex magnetic structures in Fe_2SiSe_4 with the sawtooth lattice

Feihao Pan^{1,*}, Xunwu Hu^{2,*}, Jiale Huang¹, Bingxian Shi¹, Jinchen Wang¹, Juanjuan Liu¹, Hongxia Zhang¹, Daye Xu¹, Jianfei Qin³, Hongliang Wang³, Lijie Hao³, Kun Cao², Peng Cheng^{1,†} and Dao-Xin Yao^{2,‡}

¹Laboratory for Neutron Scattering and Beijing Key Laboratory of Optoelectronic Functional Materials and MicroNano Devices, Department of Physics, Renmin University of China, Beijing 100872, China

²State Key Laboratory of Optoelectronic Materials and Technologies, Guangdong Provincial Key Laboratory of Magnetoelectric Physics and Devices, Center for Neutron Science and Technology, School of Physics, Sun Yat-sen University, Guangzhou 510275, China

³China Institute of Atomic Energy, PO Box-275-30, Beijing 102413, China



(Received 1 March 2023; accepted 9 June 2023; published 23 June 2023)

The sawtooth lattice shares some structural similarities with the kagome lattice and may attract renewed research interest. Here we report a comprehensive study on the physical properties of Fe_2SiSe_4 , an unexplored member in the olivine chalcogenides with the sawtooth lattice of Fe. Our results show that Fe_2SiSe_4 is a magnetic semiconductor with band gap of 0.66 eV. It first undergoes an antiferromagnetic transition at $T_{m1} = 110$ K, then an ferrimagneticlike one at $T_{m2} = 50$ K, and finally a magnetic transition at $T_{m3} = 25$ K, which is likely driven by the thermal populations of spin-orbit manifold on the Fe sites. Neutron diffraction analysis reveals a noncollinear antiferromagnetic structure with propagation vector $\mathbf{q}_1 = (0, 0, 0)$ at $T_{m2} < T < T_{m1}$. Interestingly, below T_{m2} , an additional antiferromagnetic structure with $\mathbf{q}_2 = (0, 0.5, 0)$ appears, and Fe_2SiSe_4 exhibits a complex double- \mathbf{q} magnetic structure which has never been observed in sawtooth olivines. Density functional theory calculations suggest this complex noncollinear magnetic structure may originate from the competing antiferromagnetic interactions for both intra- and interchain in the sawtooth lattice. Furthermore, band-structural calculations show that Fe_2SiSe_4 has quasi-flat-band features near the valence and conduction band structure. Our results have shown that Fe_2SiSe_4 could serve as a new material playground for further research on magnetic devices and the flat-band effect through chemical doping.

DOI: [10.1103/PhysRevB.107.224423](https://doi.org/10.1103/PhysRevB.107.224423)

I. INTRODUCTION

Materials with the sawtooth lattice have attracted attention from the condensed-matter physics community for several reasons. First, the sawtooth antiferromagnetic (AFM) chain with corner-sharing triangles of spins represents one of the fundamental models of geometrically frustrated quantum magnetism as that in triangular and kagome lattices [1,2]. Secondly, the sawtooth lattice also exhibits flat-band feature [3], which may give rise to high thermoelectric performance [4], quantum topological phase [5–7], flat-band spin dynamics and phonon anomalies [8]. Besides, a two-dimensional kagome lattice can be viewed as the combination of one-dimensional sawtooth chains. Therefore the recent discoveries of novel physical properties in kagome material [9–13] may generate renewed interest in sawtooth material, since these two kinds share structural similarities and connections.

The A_2BX_4 ($A = \text{Mn, Fe, Ni}$; $B = \text{Si, Ge}$; $X = \text{O, S, Se, Te}$) olivines represent a large material family where the transitional-metal atoms form a sawtooth lattice. Most members in this series are ferrimagnets or antiferromagnets whose

spin structure could be described by magnetic propagation vector $\mathbf{q} = (0,0,0)$ [14,15]. Among them, magnetic frustration is observed for Mn_2SiSe_4 [16]. Mn_2SiS_4 and Mn_2GeS_4 are reported to exhibit anomalous magnetic properties resulting from the quantum fluctuations near a spin-flop bicritical point [17]. Mn_2GeO_4 is identified as a functional material that exhibits coupled ferromagnetism and ferroelectricity [18]. Fe_2GeS_4 and Fe_2GeSe_4 are theoretically proposed as promising candidates with good thermoelectric performance due to their quasi-flat-band feature [4]. These findings highlight the exotic physical properties which are closely related to the peculiar sawtooth lattice.

In the A_2BX_4 series, we noticed that although the magnetic properties of Fe_2SiO_4 and Fe_2SiS_4 have been reported [15,19], Fe_2SiSe_4 remains an unexplored member whose chemical phase is even missing in the current inorganic crystal structure database (ICSD). So it would be interesting to check whether the Fe_2SiSe_4 phase with sawtooth lattice really exists. In this paper we report the synthesis of Fe_2SiSe_4 single crystals, which is characterized by the sawtooth lattice of Fe. Using magnetization, heat capacity, neutron-scattering techniques, and band-structure calculations, Fe_2SiSe_4 is identified as a magnetic semiconductor with multiple magnetic transitions, noncollinear double- \mathbf{q} magnetic structures, and as quasi-flat-band. The underlying physical mechanism for the magnetic properties and potential applications of Fe_2SiSe_4

*These authors contributed equally to this work.

†Corresponding author: pcheng@ruc.edu.cn

‡Corresponding author: yaodaoy@mail.sysu.edu.cn

are discussed combined with the results of density-functional theory (DFT) calculations.

II. EXPERIMENTAL METHODS

Single crystals of Fe_2SiSe_4 were grown by the chemical vapor transport method. The pure powders of Fe, Si, and Se were mixed in molar ratio 1:2:4 (total mass 1 g) and placed into a quartz tube (inner diameter of 12 mm, length 10 cm) with 100 mg iodine. Then the quartz tube was evacuated to 3.0×10^{-3} Pa and sealed before being put into a two-zone tube furnace. The quartz tube was heated to 590°C in the raw material end and 660°C in the other end in 750 min, then maintained at those temperatures for 5760 min. The next step is a so-called “temperature reversing process” in which the two ends switch temperatures in 70 min and are held in the new temperatures for 12.5 days before being cooled with the furnace. The shining black single crystals of Fe_2SiSe_4 appeared in the final cold end with typical dimensions of $1 \text{ mm} \times 2 \text{ mm} \times 0.5 \text{ mm}$.

X-ray diffraction (XRD) patterns of powder samples were collected from a Bruker D8 Advance x-ray diffractometer using Cu $K\alpha$ radiation. Magnetization measurements were carried out in Quantum Design MPMS3. Resistivity and heat capacity of the samples were measured on Quantum Design PPMS-14T. The powder neutron diffraction experiments were carried out on Xingzhi cold neutron triple-axis spectrometer at the China Advanced Research Reactor (CARR). For neutron experiments on Xingzhi, the incident neutron energy was fixed at 16 meV with a neutron velocity selector used upstream to remove higher-order neutrons [20]. About 3 g Fe_2SiSe_4 powders (crushed from single crystals) were used in neutron experiments. The FULLPROFSUITE program package was used in the Rietveld refinement of neutron powder diffraction data [21,22], and the software SARAH was used for the representational analysis [23].

The electronic structure and magnetic properties calculations were performed using the DFT as implemented in the Vienna *ab initio* simulation package (VASP) code [24,25]. The generalized gradient approximation (GGA) in the form of a Perdew-Burke-Ernzerhof (PBE) [26] functional was used for exchange correlation. The projector-augmented-wave (PAW) method [27] with a 300-eV plane-wave cutoff energy was employed. The valence electron configurations for each atom were $3d^7 4s^1$ for Fe, $3s^2 3p^2$ for Si, and $3d^{10} 4s^2 4p^4$ for Se. A Γ -centered $3 \times 2 \times 5$ k -point mesh within the Monkhorst-Pack scheme was used for Brillouin-zone sampling. The Hubbard U [28] for the $3d$ electrons of Fe was chosen as 2 eV to reproduce the experimental magnetic moments and band gap of Fe_2SiSe_4 . A $1 \times 2 \times 1$ supercell was adopted due to the noncollinear AFM structure. The direction of the magnetic moment was constrained, that is, the superimposed double- \mathbf{q} magnetic structure was adopted. All calculations were performed using the experimental structural parameters. Convergence criteria employed for both the electronic self-consistent iteration and the ionic relaxation were set to 10^{-6} eV and 0.01 eV/Å, respectively. Heisenberg exchange interactions were calculated by the four-states method [29]. A $1 \times 2 \times 2$ supercell was adopted to avoid spurious interaction by the periodic boundary conditions.

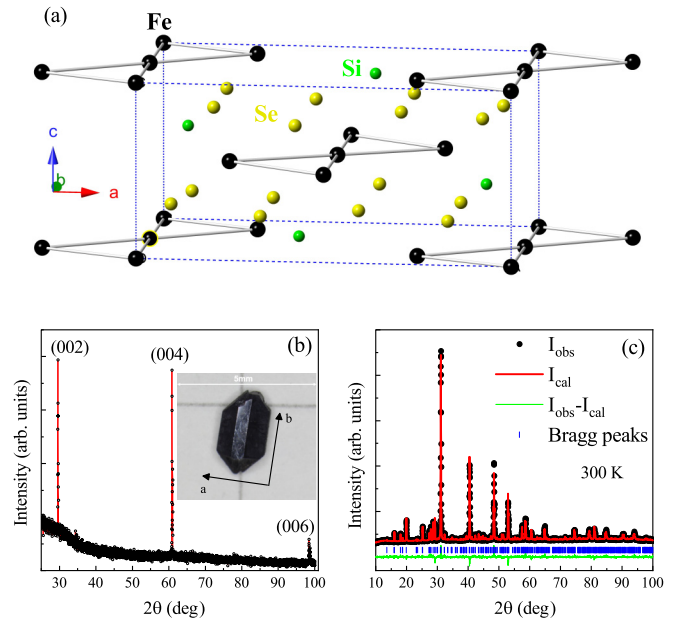


FIG. 1. (a) Crystal structure of Fe_2SiSe_4 . The Fe-Fe bond is plotted to demonstrate five Fe sawtooth chains. (b) The x-ray reflections from the ab plane of Fe_2SiSe_4 single crystal. The inset shows the photo of one crystal. (c) Room-temperature XRD patterns of powders (crushed from single crystals) and the Rietveld refinement results.

III. RESULTS AND DISCUSSION

A. Crystal structure and magnetization

In Fig. 1(c), the XRD patterns on powder samples (crushed from single crystals) and Rietveld refinement confirm Fe_2SiSe_4 adopts the orthorhombic symmetry with space group $Pnma$ (No. 62), which belongs to the olivine-type structure, same as Fe_2SiS_4 and Fe_2SiO_4 [14,15]. The obtained lattice parameters are $a = 13.020 \text{ \AA}$, $b = 7.544 \text{ \AA}$ and $c = 6.119 \text{ \AA}$. The x-ray reflection pattern from the ab plane of Fe_2SiSe_4 single crystal in Fig. 1(b) also confirms the above results. As shown in Fig. 1(a), the Fe atoms form infinite sawtooth chains along the b axis.

The Laue diffraction patterns allow us to distinguish the major crystal axes with respect to the three-dimensional shape of Fe_2SiSe_4 single crystal. So the temperature-dependent magnetization along the a , b , and c axis were performed, respectively; the results are shown in Fig. 2. Three successive magnetic transitions could be identified. At $T_{m1} = 110 \text{ K}$, a cusp appears which is most prominent under $H \parallel b$, indicating an AFM transition. At lower temperatures, a second magnetic transition occurs at $T_{m2} = 50 \text{ K}$. Its temperature-dependent magnetization behavior seems to be AFM-like under $H \parallel b$ while being ferromagneticlike along other field directions. Then at $T_{m3} = 25 \text{ K}$, the magnetization anomalies along all three directions suggest the existence of a third magnetic transition.

The temperature-dependent magnetization shows strong anisotropic behavior along three different directions. Even in the paramagnetic region, the magnetization under $H \parallel a$ or $H \parallel c$ exhibits typical Curie-Weiss (CW) behavior while that under $H \parallel b$ shows an anomalous linear temperature

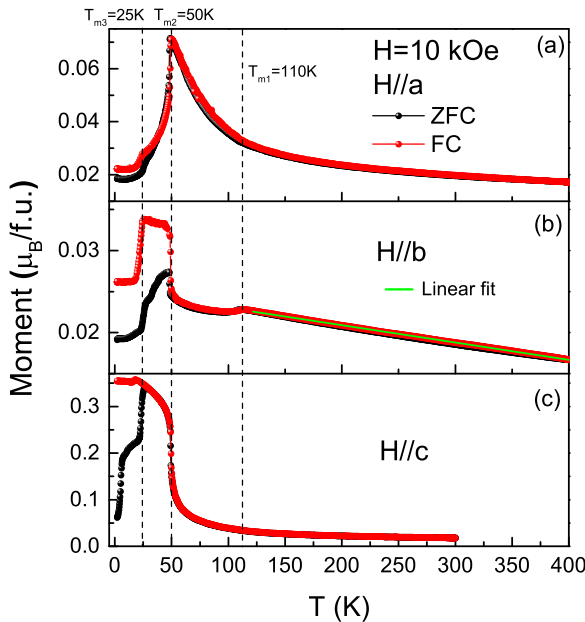


FIG. 2. Temperature-dependent magnetizations with applied field along the a , b , and c axis are shown respectively in (a), (b), and (c).

dependence up to 400 K. The CW fit of the high-temperature magnetization data yields $\mu_{\text{eff}}/\text{Fe} = 4.02 \mu_B$ and $\theta_{\text{CW}} = -66$ K for $H \parallel a$, $\mu_{\text{eff}}/\text{Fe} = 4.08 \mu_B$, and $\theta_{\text{CW}} = -51$ K for $H \parallel c$. This result indicates dominant antiferromagnetic correlations in Fe_2SiSe_4 . Meanwhile the derived effective moment is obviously smaller than the theoretical value $4.90 \mu_B/\text{Fe}^{2+}$ without orbital contribution. This discrepancy gives rise to a question of whether CW fitting could be applied to Fe_2SiSe_4 or the fitting results could be interpreted in the conventional way. Specifically, the abnormal high-temperature T-linear magnetization exists for $H \parallel b$. Similar behavior was observed in Fe-based superconductors and parent compounds [30–32], which is explained as a result of AFM spin fluctuations in the normal state [33]. Further theoretical works are needed to check whether this explanation applies to Fe_2SiSe_4 .

B. Magnetic structure

Since the T-dependent magnetization indicates the existence of three possible magnetic transitions, powder neutron diffraction on Fe_2SiSe_4 was performed at 150, 80, 35, and 3.5 K to determine the magnetic structure. As shown in Fig. 3, the Bragg peaks at 150 K could be well indexed by the nuclear scattering with high-quality refining parameters. At 80 K, magnetic contributions and peaks can be easily identified near $2\theta = 22^\circ$ and 35° . Detailed analysis using FULLPROF software [21,22] shows that all magnetic reflections overlap with the nuclear reflections (except for some nuclear peaks with diffraction extinction) and could be well defined by the propagation vector $\mathbf{q}_1 = (0, 0, 0)$. Figure 4(b) shows that the intensities of Bragg peak (0,0,1) could be served as the magnetic order parameter for the first AFM transition at $T_{m1} = 110$ K.

Below $T_{m2} = 50$ K, new magnetic peaks with half integer are identified (Fig. 3). As shown in Fig. 4(b), the

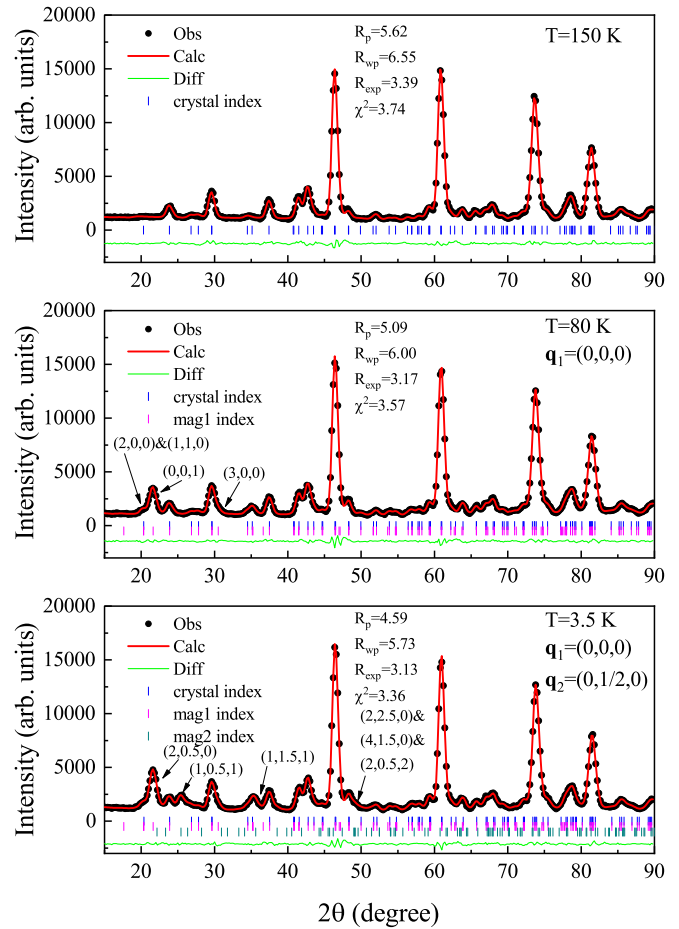


FIG. 3. The powder neutron diffraction spectra and Rietveld refinement results for Fe_2SiSe_4 at 150, 80, and 3.5 K. Some of the magnetic peaks are labeled with arrows.

temperature-dependent intensity of (1,0,5,1) signifies new magnetic order develops below T_{m2} . It should be noted there is almost no difference for the diffraction patterns at 35 and 3.5 K within our instrumental resolution. Therefore the magnetic transition T_{m3} may not change the zero-field magnetic structure.

The identification of considerable magnetic peaks allows us to determine the magnetic structures at different temperatures through Rietveld refinement. The detailed representational analysis and refinement process are presented in the Supplemental Material [34]. The magnetic structures resolved from the best fit are plotted in Fig. 4 and are discussed in detail.

First of all, at 80 K the noncollinear AFM structure with magnetic wave vector $\mathbf{q}_1 = (0, 0, 0)$ is identified and illustrated in Fig. 4(a). The Fe ions occupy two inequivalent Wyckoff positions. We label those at the $4a$ site as Fe1 (black spheres) and those at $4c$ sites as Fe2 (gray spheres). The magnetic moments all lie in the ab plane, and the data refinement yields a total moment of $1.45 \mu_B/\text{Fe}$ for Fe1 and $4.04 \mu_B/\text{Fe}$ for Fe2. The latter points parallel to the b axis while the former is canted to the a axis to a certain degree. This magnetic structure is quite similar as that in olivine-type Fe_2SiO_4 and Fe_2SiS_4 [14,15]. Therefore, similar physical interpretations

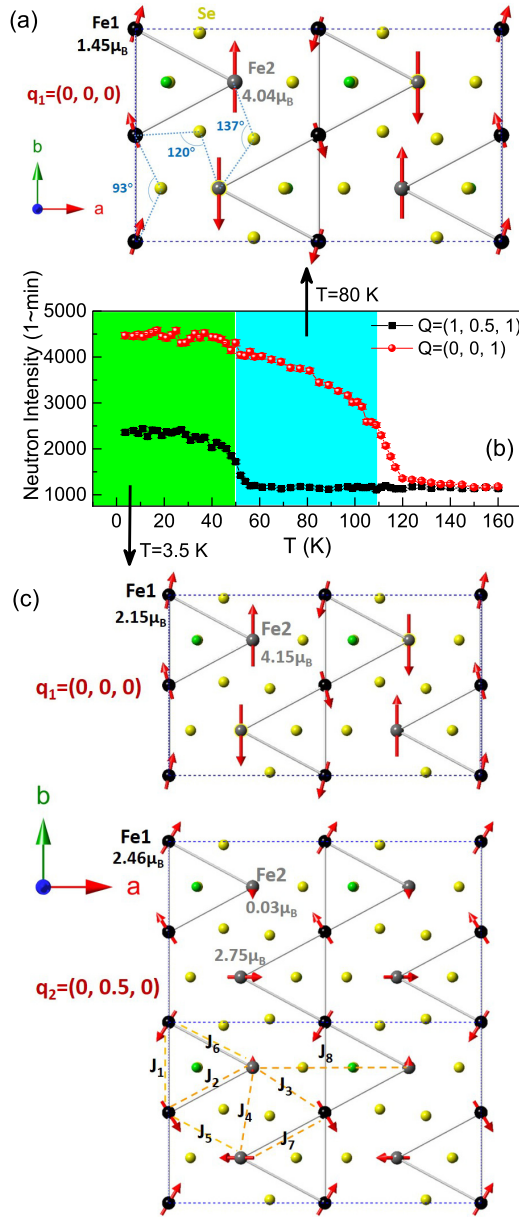


FIG. 4. (a) Schematics of refined magnetic structure of Fe_2SiSe_4 at 80 K. (b) The temperature-dependent intensities of magnetic peaks (0,0,1) and (1,0.5,1). (c) The refined magnetic structures of Fe_2SiSe_4 at 3.5 K with different propagation vectors are illustrated.

of this magnetic structure considering the indirect superexchange interactions between Fe cations via Se atoms could be given. As marked in Fig. 4(a), the Fe2-Se-Fe2 angle is closer to 180° and gives rise to a strong AFM interaction, while the angle of Fe1-Se-Fe1 is much smaller, which may largely reduce the AFM interaction [15]. A competition between crystal-field anisotropy and AFM exchange via spin-orbit coupling results in the canting of Fe1 moments [14].

Secondly, at 3.5 K the above magnetic model with $\mathbf{q}_1 = (0, 0, 0)$ can only partially fit the neutron diffraction patterns and could not explain new magnetic peaks with half integers appearing below T_{m2} (Fig. 3). The most prominent one is indexed as (1,0.5,1), whose temperature-dependent intensities

TABLE I. Calculated magnetic exchange coupling constants between different Fe sites, positive value means AFM coupling.

Constant	J_1	J_2	J_3	J_4	J_5	J_6	J_7	J_8
Value (meV)	8	9	15	12	15	9	8	0.3

are shown in Fig. 4(b). The new magnetic peaks developed below T_{m2} can be well defined by a new propagation vector $\mathbf{q}_2 = (0, 0.5, 0)$. We found that only a combined model which includes both the magnetic structure with \mathbf{q}_1 and that with \mathbf{q}_2 could achieve a good fit to the data collected at 3.5 K. The refined two magnetic structures with different wave vectors are illustrated in Fig. 4(c). One can see that the one with \mathbf{q}_1 is quite similar as that at 80 K, except for a slightly increased ordered moment and different canting angle for the Fe1 moment. The magnetic structure with \mathbf{q}_2 is also noncollinear and more complex; the magnetic unit cell is doubled along the b axis. The moments of Fe2 have two different values, and one of them is almost negligible ($0.03 \mu_B$).

The magnetic order at 3.5 K has two different propagation wave vectors. These two modulations may either reside in different domains independently, known as the multidomain state, or coexist in a single domain in the form of a superimposed double- \mathbf{q} state. These two states may be indistinguishable in diffraction experiments performed on powder samples. The multi- \mathbf{q} magnetic order is not a common case in magnetic material. Some famous examples include a double- \mathbf{q} spin-density wave in the Fe-based superconductor $\text{Sr}_{1-x}\text{Na}_x\text{Fe}_2\text{As}_2$ with tetragonal crystal symmetry [35] and triple- \mathbf{q} magnetic state in $\text{Na}_2\text{Co}_2\text{TeO}_6$ with hexagonal crystal symmetry [36]. For Fe_2SiSe_4 , whether there is a double-domain state or a double- \mathbf{q} state, this state in an orthorhombic crystal symmetry is particularly rarely observed.

To explore the underlying mechanism for the complex magnetic structure of Fe_2SiSe_4 at 3.5 K, we investigate its exchange couplings based on a simple Heisenberg model:

$$H = \sum_{i < j} J_{ij} S_i S_j. \quad (1)$$

Our DFT calculations reveal the values of exchange coupling constant J_i between Fe ions at different sites [illustrated in Fig. 4(c)], and the results are listed in Table I. We can see that all of the J_i values are positive, which means each side of the sawtooth chains are AFM coupling. The intrachain exchange coupling J_1 , J_2 , J_6 , and J_7 are connected by an exchange path Fe-Si-Se-Fe with distance $d(J_1) = 3.78 \text{ \AA}$. The interchain exchange couplings J_3 , J_4 , J_5 are instead realized through the exchange path Fe-Se-Se-Fe with the distance $d(J_4) = 4.89 \text{ \AA}$. Furthermore, the exchange coupling values of interchain are almost twice as large as those of intrachain. This is probably due to the strong hybridization of Se $4p$ and Fe $3d$ orbitals near the Fermi level. A very large Fe-Fe distance $d(J_8) = 7.17 \text{ \AA}$ results in a much weaker magnetic interaction. Therefore the competition of AFM interactions on different sides of the sawtooth chain combined with the interchain exchange interaction may be responsible for a complex noncollinear double- \mathbf{q} magnetic order in Fe_2SiSe_4 . Based on this model, we employ a superimposed double- \mathbf{q} magnetic structure to

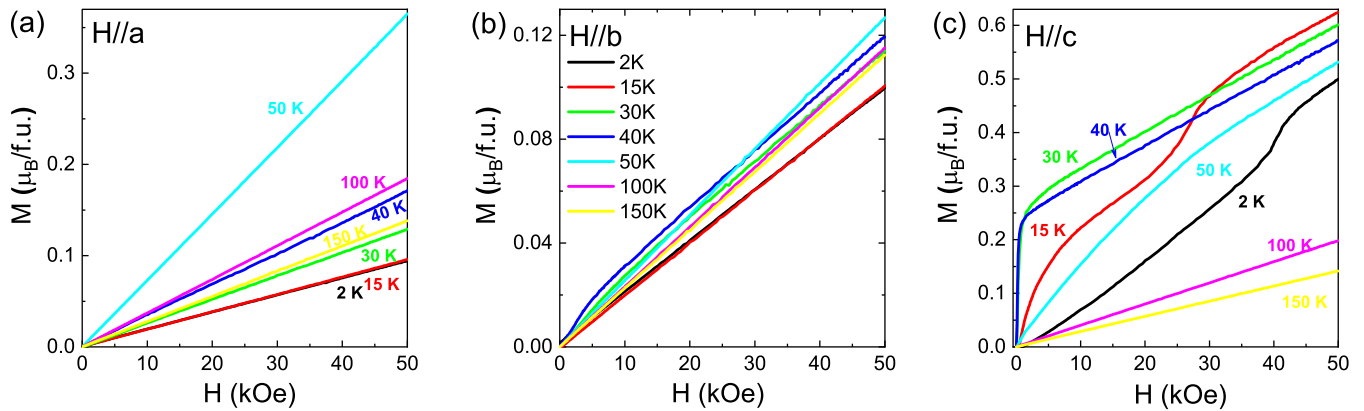


FIG. 5. Isothermal magnetizations under magnetic field applied along the *a*, *b*, and *c* axes at selected temperatures are shown.

constrain the direction of the magnetic moment. The calculated spin configuration at low temperature of Fe_2SiSe_4 is shown in Table S9 and is qualitatively consistent with the superimposed double- \mathbf{q} magnetic structure determined experimentally (Table S8).

C. Isothermal magnetization, AC susceptibility, and heat capacity

Further measurements on Fe_2SiSe_4 single crystal were performed to get insights on its magnetic state. As shown in Fig. 5, the isothermal magnetizations under $H \parallel a$ and $H \parallel b$ are linear with increasing field for most temperatures, which is consistent with an AFM state. Nevertheless, for $H \parallel c$, a nonlinear $M(H)$ curve appears below $T_{m2} = 50$ K. Especially for 30- and 40-K data, they first show a ferromagneticlike fast magnetization to about $0.13 \mu_B/\text{Fe}$ at low field then increase linearly with field. This fast magnetization seems to gradually disappear below $T_{m3} = 25$ K. The above observations suggest the magnetic transition at T_{m2} is a ferrimagnetic one. The magnetic hysteresis behavior at 35 K in Fig. 6(a) and the peak in the imaginary part of AC susceptibility χ'' at T_{m2} [Fig. 6(b)] further support this conclusion.

In the previous section, the double- \mathbf{q} magnetic structure below T_{m2} identified from neutron diffraction is actually antiferromagnetlike without a net moment component in any direction. This seems to contradict the ferrimagnetic behavior observed in magnetization measurements. The explanation might be that the net magnetization $0.13 \mu_B/\text{Fe}$ observed in Fig. 5(c) is quite small. This small ferrimagnetic component is not easily detected due to the neutron instrumental resolution. We also need to point out that the moment of Fe has no component along the *c* axis at 80 K, but Fe2 actually has a *c*-axis component of $1.14 \mu_B$ at 3.5 K, which can be seen from Tables S7 and S8. This indicates the magnetic anisotropy has notable change below T_{m2} .

Another question that needs to be answered is the nature of magnetic transition at $T_{m3} = 25$ K. The experimentally measured specific heat of Fe_2SiSe_4 is shown in Fig. 7. From the raw data $C_p(T)$, the magnetic transitions at T_{m1} and T_{m2} can be identified by the jumps, while there is no detectable feature at T_{m3} . Then, if using an Einstein-model-based curve to account for the phonon part of the specific heat, we can obtain the magnetic specific heat C_{mag} shown by the blue

curve in Fig. 7. The $C_{\text{mag}}(T)$ shows a shoulder at $T_{m3} = 25$ K. The inset of Fig. 7 shows the calculated magnetic entropy of Fe_2SiSe_4 as compared with the limiting value $2R \ln 5$ by assuming the spin-orbit manifold is fully occupied and there are $2S + 1 = 5$ equally occupied states for each Fe^{2+} . It should be noted that we have failed to synthesize samples with possible Zn_2SiSe_4 phase for a more accurate phonon estimation. We also have tried to use the Debye model or an amalgamation

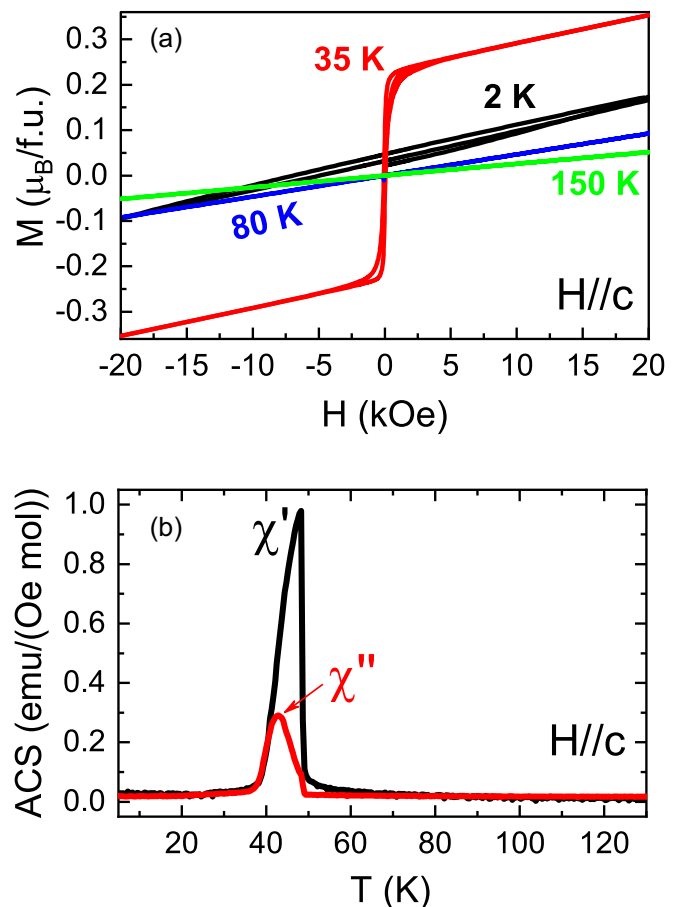


FIG. 6. (a) Magnetic hysteresis under $H \parallel c$ for Fe_2SiSe_4 at selected temperatures. (b) The temperature-dependent AC susceptibilities measured under an oscillated AC field of 5.0 Oe applied along the *c* axis.

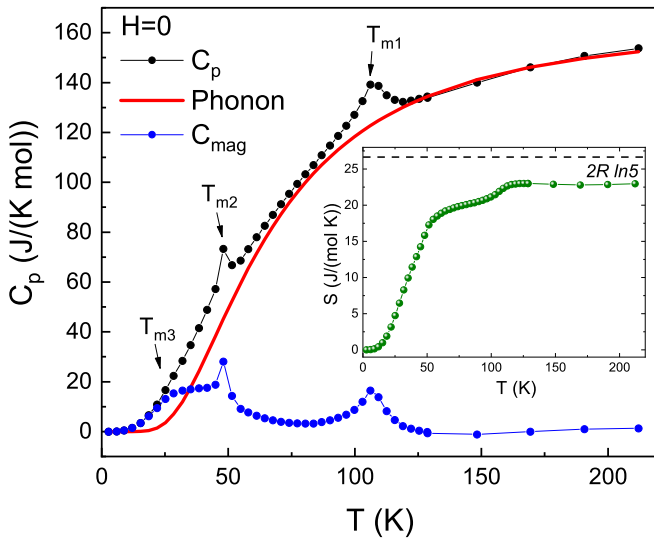


FIG. 7. Temperature-dependent specific heat of Fe_2SiSe_4 . The magnetic specific heat C_{mag} is derived by subtracting phonon contributions through an Einstein-model-based curve fit on the data above 110 K. Then the calculated magnetic entropy is shown in the inset.

of both Einstein and Debye models to estimate the phonon contribution. All results have shown a similar shoulderlike feature at T_{m3} in $C_{\text{mag}}(T)$, and the Debye model gives lower magnetic entropy value ($17.3 \text{ J mol}^{-1} \text{ K}^{-1}$ at 120 K).

We found this shoulderlike transition also exists in isostructural Fe_2SiO_4 at similar temperature (20 K), and its origin has been uncovered as a Schottky anomaly arising from the spin-orbit manifold of the Fe^{2+} ion [19]. To be specific, for Fe_2SiO_4 , Aronson *et al.* found that the lowest crystal-field splitting t_{2g} level is further split into five states due to spin-orbit coupling. These spin-orbit energy levels are determined through inelastic neutron experiments and have a dominant influence on the low-temperature physical properties. Then the shoulder in specific heat can be quantitatively

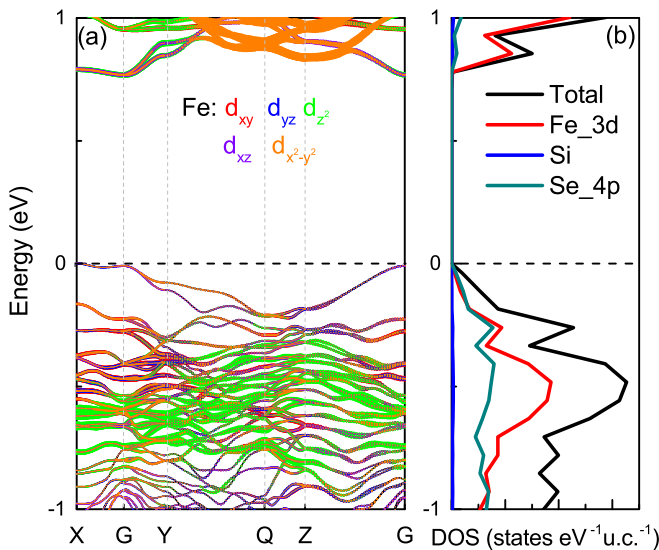


FIG. 8. Calculated band structure (a), total and projected density of states (b) of Fe_2SiSe_4 .

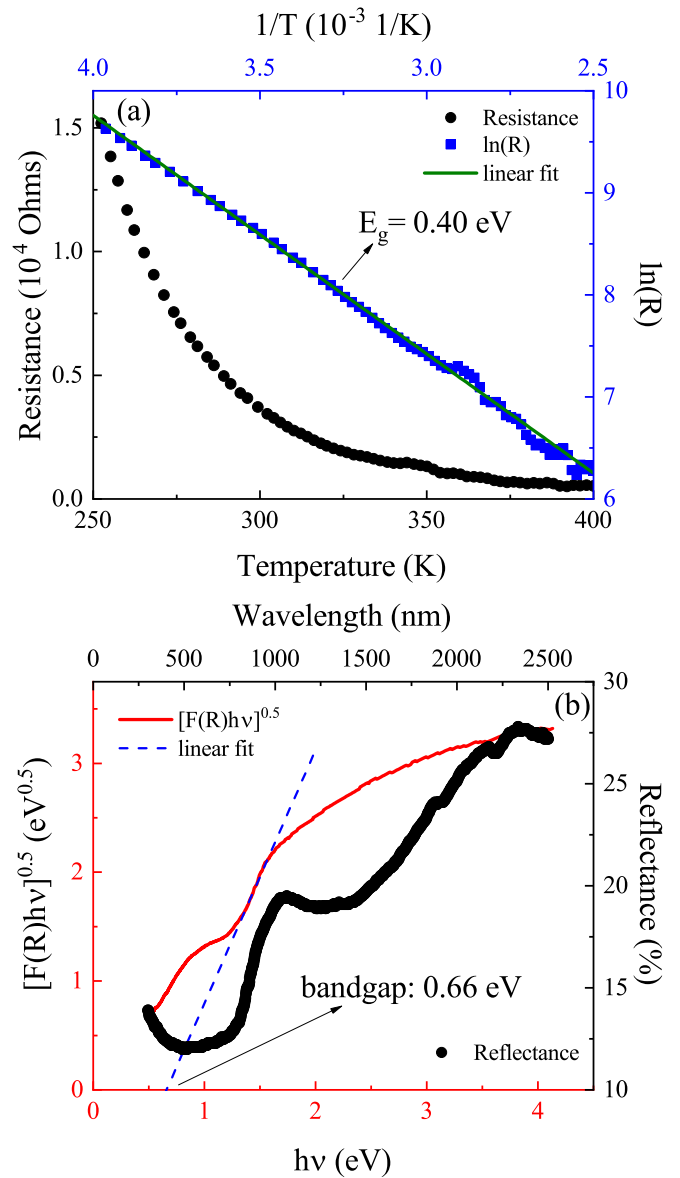


FIG. 9. (a) The temperature-dependent resistance of Fe_2SiSe_4 . (b) The diffusion reflectance spectroscopy of the Fe_2SiSe_4 powder sample (top and right coordinates) and the plot of $[F(R)hv]^{0.5}$ vs photoenergy hv (bottom and left coordinates).

calculated and simulated by a Schottky anomaly arising from the spin-orbit excitations [19]. This explanation may also apply to the anomalous magnetic transition at T_{m3} for Fe_2SiSe_4 . On the other hand, Considering the absence of a visible $C_p(T)$ anomaly at T_{m3} and the discrepancy between zero-field-cooled and field-cooled magnetic susceptibility below T_{m3} , it is also plausible that the T_{m3} anomaly arises from spin glass phenomena.

The thermal population in different spin-orbital states may drastically change across T_{m3} , which leads to rich magnetic behaviors in Fe_2SiSe_4 . As demonstrated in Figs. 5 and 6, the magnetization switches from AFM to ferromagnetic behavior then back to AFM behavior as decreasing temperature. In addition, magnetic-field-induced spin-flop transitions are also observed for the $M(H)$ curve at 15 and 2 K under

$H \parallel c$. Combined with the semiconductor nature of this compound, which will be discussed in the next section, Fe_2SiSe_4 may find applications in optoelectronics and magnetic devices.

D. Band structure

The sawtooth lattice is known to have flat bands similar to the kagome lattice. The band structure of Fe_2SiSe_4 obtained by DFT calculations is shown in Fig. 8. The result reveals that Fe_2SiSe_4 is a semiconductor with an indirect band gap of 0.7 eV. The gap value is close to that determined from experiment. As demonstrated in Fig. 9(a), the temperature-dependent resistance of Fe_2SiSe_4 shows a typical semiconducting behavior, and the value is beyond the instrument limit below 250 K. Through fitting the resistance data using the thermal activation model as described by $R(T) = R_0 e^{(E_g/2k_B T)}$, a band gap $E_g = 0.40$ eV could be obtained. The diffusion reflectance spectroscopy of Fe_2SiSe_4 was also measured to check the band gap. The data are presented in Fig. 9(b), and an absorption band at around 800 nm is detected. The plot of $[F(R)h\nu]^{0.5}$ versus photo energy $h\nu$ is also shown in the figure. $F(R)$ is the Kubella-Munk function, defined as $[F(R)h\nu]^{0.5}$ [37]. R is the experimentally observed reflectance. Using the methods proposed in [37,38], the band gap of Fe_2SiSe_4 is calculated to be 0.66 eV, which agrees well with the DFT calculated value.

From Fig. 8(a), Fe_2SiSe_4 is found to have flat bands from the G-X crystallographic direction, similar to other sawtooth materials such as Mn_2SiSe_4 and Fe_2GeSe_4 [4,16]. The corresponding total and projected density of states (DOS) for Fe_2SiSe_4 are shown in Fig. 8(b). The states near the Fermi level mainly come from the contributions from Fe $3d$ states and Se $4p$ states. Strong hybridization of Se $4p$ and Fe $3d$ orbitals could be observed below the Fermi level.

For kagome metals where the flat band is quite close to the Fermi level, novel properties including emergent ferromagnetism, anomalous Hall effect, superconductivity, and topological phases have been extensively reported in recent years [9–11,39–42]. We find the band gap of Fe_2SiSe_4 is not

large; there are possibilities that one could use pressure or chemical doping to tune it into a metal. Then it would be worthwhile to check whether a quasi-flat-band near Fermi level would enable realization of other versatile quantum phenomena.

IV. CONCLUSIONS

In summary, we present a comprehensive study on the sawtooth lattice chalcogenide olivines Fe_2SiSe_4 . This material has shown intriguing magnetic properties. Three magnetic transitions are identified: an AFM one at 110 K, a ferrimagnetic one at 50 K, and the last one at 25 K, possibly due to the spin-orbit excitation. We determined the magnetic structures at different temperatures through neutron diffraction and discovered a noncollinear double- \mathbf{q} magnetic order below 50 K. DFT calculations suggest this complex magnetic structure may be due to the competition of AFM interactions on different sides of the sawtooth chain combined with the interchain exchange interaction. Through band-structure calculation and spectral experiments, Fe_2SiSe_4 was identified as a magnetic semiconductor with an indirect band gap of 0.66 eV and quasi-flat-band. We propose that Fe_2SiSe_4 may provide a new material playground for further research on magnetic devices and the flat-band effect through chemical doping.

ACKNOWLEDGMENTS

This work was supported by the National Natural Science Foundation of China (through Grants No. 12074426, No. 12004426, No. 11974432, and No. 92165204), the National Key Research and Development Program of China (through Grants No. 2018YFA0306001 and No. 2022YFA1402802), Shenzhen International Quantum Academy (Grant No. SIQA202102), National Key Scientific Instrument and Equipment Development Project of NSFC (Grant No. 11227906), the Fundamental Research Funds for the Central Universities, and the Research Funds of Renmin University of China (Grant No. 22XNKJ40), NSAF (Grant No. U2030106).

-
- [1] I. S. Hagemann, P. G. Khalifah, A. P. Ramirez, and R. J. Cava, Geometric magnetic frustration in olivines, *Phys. Rev. B* **62**, R771 (2000).
- [2] G. C. Lau, B. G. Ueland, R. S. Freitas, M. L. Dahlberg, P. Schiffer, and R. J. Cava, Magnetic characterization of the sawtooth-lattice olivines ZnL_2S_4 ($L = \text{Er}, \text{Tm}, \text{Yb}$), *Phys. Rev. B* **73**, 012413 (2006).
- [3] Sebastian D. Huber and Ehud Altman, Bose condensation in flat bands, *Phys. Rev. B* **82**, 184502 (2010).
- [4] V. K. Gudelli, V. Kanchana, and G. Vaitheeswaran, Predicted thermoelectric properties of olivine-type Fe_2GeCh_4 ($\text{Ch} = \text{S}, \text{Se}$ and Te), *J. Phys.: Condens. Matter* **28**, 025502 (2016).
- [5] S. A. Blundell and M. D. Núñez-Regueiro, Quantum topological excitations: From the sawtooth lattice to the Heisenberg chain, *Eur. Phys. J. B* **31**, 453 (2003).
- [6] Y. Yang, S.-J. Ran, X. Chen, Z.-Z. Sun, S.-S. Gong, Z. Wang, and G. Su, Reentrance of the topological phase in a spin-1 frustrated Heisenberg chain, *Phys. Rev. B* **101**, 045133 (2020).
- [7] H. Yang, H. Nakano, and H. Katsura, Symmetry-protected topological phases in spinful bosons with a flat band, *Phys. Rev. Res.* **3**, 023210 (2021).
- [8] V. P. Gnezdilov, Yu. G. Pashkevich, V. S. Kurnosov, O. V. Zhuravlev, D. Wulferding, P. Lemmens, D. Menzel, E. S. Kozlyakova, A. Yu. Akhrovov, E. S. Kuznetsova, P. S. Berdonosov, V. A. Dolgikh, O. S. Volkova, and A. N. Vasiliev, Flat-band spin dynamics and phonon anomalies of the sawtooth spin-chain system $\text{Fe}_2\text{O}(\text{SeO}_3)_2$, *Phys. Rev. B* **99**, 064413 (2019).
- [9] Z. Lin, J.-H. Choi, Q. Zhang, W. Qin, S. Yi, P. Wang, L. Li, Y. Wang, H. Zhang, Z. Sun, L. Wei, S. Zhang, T. Guo, Q. Lu, J.-H. Cho, C. Zeng, and Z. Zhang, Flatbands and Emergent Ferromagnetic Ordering in Fe_3Sn_2 Kagome Lattices, *Phys. Rev. Lett.* **121**, 096401 (2018).

- [10] Q. Wang, Y. Xu, R. Lou, Z. Liu, M. Li, Y. Huang, D. Shen, H. Weng, S. Wang, and H. Lei, Large intrinsic anomalous Hall effect in half-metallic ferromagnet $\text{Co}_3\text{Sn}_2\text{S}_2$ with magnetic Weyl fermions, *Nat. Commun.* **9**, 3681 (2018).
- [11] B. R. Ortiz, S. M. L. Teicher, Y. Hu, J. L. Zuo, P. M. Sarte, E. C. Schueller, A. M. M. Abeykoon, M. J. Krogstad, S. Rosenkranz, R. Osborn, R. Seshadri, L. Balents, J. He, and S. D. Wilson, CsV_3Sb_5 : A \mathbb{Z}_2 Topological Kagome Metal with a Superconducting Ground State, *Phys. Rev. Lett.* **125**, 247002 (2020).
- [12] L. Nie, K. Sun, W. Ma, D. Song, L. Zheng, Z. Liang, P. Wu, F. Yu, J. Li, M. Shan, D. Zhao, S. Li, B. Kang, Z. Wu, Y. Zhou, K. Liu, Z. Xiang, J. Ying, Z. Wang, T. Wu *et al.*, Charge-density-wave-driven electronic nematicity in a kagome superconductor, *Nature (London)* **604**, 59 (2022).
- [13] Q. Yin, Z. Tu, C. Gong, Y. Fu, S. Yan, and H. Lei, Superconductivity and normal-state properties of kagome metal RbV_3Sb_5 single crystals, *Chin. Phys. Lett.* **38**, 037403 (2021).
- [14] H. Ehrenberg and H. Fuess, Analytical interpretation and simulation of the static magnetic properties of synthetic $\alpha\text{-Fe}_2\text{SiO}_4$, *J. Phys.: Condens. Matter* **5**, 3663 (1993).
- [15] V. Baron, Ö. Amcoff, and T. Ericsson, Neutron powder diffraction study of the crystal and magnetic structures of Fe_2SiS_4 , *J. Magn. Magn. Mater.* **195**, 81 (1999).
- [16] H. Nhalil, R. Baral, B. O. Khamala, A. Cosio, S. R. Singamaneni, M. Fitta, D. Antonio, K. Gofryk, R. R. Zope, T. Baruah, B. Saparov, and H. S. Nair, Antiferromagnetism and the emergence of frustration in the sawtooth lattice chalcogenide olivines $\text{Mn}_2\text{SiS}_{4-x}\text{Se}_x$ ($x = 0 - 4$), *Phys. Rev. B* **99**, 184434 (2019).
- [17] K. Ohgushi and Y. Ueda, Anomalous Magnetic Properties near the Spin-Flop Bicritical Point in Mn_2AS_4 ($A = \text{Si}$ and Ge), *Phys. Rev. Lett.* **95**, 217202 (2005).
- [18] J. S. White, T. Honda, K. Kimura, T. Kimura, Ch. Niedermayer, O. Zaharko, A. Poole, B. Roessli, and M. Kenzelmann, Coupling of Magnetic and Ferroelectric Hysteresis by a Multicomponent Magnetic Structure in Mn_2GeO_4 , *Phys. Rev. Lett.* **108**, 077204 (2012).
- [19] M.C. Aronson, L. Stixrude, M. K. Davis, W. Gannon, and K. Ahilan, Magnetic excitations and heat capacity of fayalite, Fe_2SiO_4 , *Am. Mineral.* **92**, 481 (2007).
- [20] P. Cheng, H. Zhang, W. Bao, A. Schneidewind, P. Link, A.T.D. Grünwald, R. Georgii, L.J. Hao, and Y.T. Liu, Design of the cold neutron triple-axis spectrometer at the China Advanced Research Reactor, *Nucl. Instrum. Methods Phys. Res., Sect. A* **821**, 17 (2016).
- [21] J. Rodríguez-Carvajal, Recent advances in magnetic structure determination by neutron powder diffraction, *Phys. B: Condens. Matter.* **192**, 55 (1993).
- [22] H. M. Rietveld, A profile refinement method for nuclear and magnetic structures, *J. Appl. Crystallogr.* **2**, 65 (1969).
- [23] A.S Wills, A new protocol for the determination of magnetic structures using simulated annealing and representational analysis (SARAh), *Phys. B: Condens. Matter* **276**, 680 (2000).
- [24] G. Kresse and J. Hafner, *Ab initio* molecular dynamics for liquid metals, *Phys. Rev. B* **47**, 558 (1993).
- [25] G. Kresse and J. Furthmüller, Efficient iterative schemes for *Ab initio* total-energy calculations using a plane-wave basis set, *Phys. Rev. B* **54**, 11169 (1996).
- [26] J. P. Perdew, K. Burke, and M. Ernzerhof, Generalized Gradient Approximation Made Simple, *Phys. Rev. Lett.* **77**, 3865 (1996).
- [27] P. E. Blöchl, Projector augmented-wave method, *Phys. Rev. B* **50**, 17953 (1994).
- [28] S. L. Dudarev, G. A. Botton, S. Y. Savrasov, C. J. Humphreys, and A. P. Sutton, Electron-energy-loss spectra and the structural stability of nickel oxide: An LSDA+U study, *Phys. Rev. B* **57**, 1505 (1998).
- [29] H. J. Xiang, E. J. Kan, S.-H. Wei, M.-H. Whangbo, and X. G. Gong, Predicting the spin-lattice order of frustrated systems from first principles, *Phys. Rev. B* **84**, 224429 (2011).
- [30] X. F. Wang, T. Wu, G. Wu, H. Chen, Y. L. Xie, J. J. Ying, Y. J. Yan, R. H. Liu, and X. H. Chen, Anisotropy in the Electrical Resistivity and Susceptibility of Superconducting BaFe_2As_2 Single Crystals, *Phys. Rev. Lett.* **102**, 117005 (2009).
- [31] J.-Q. Yan, A. Kreyssig, S. Nandi, N. Ni, S. L. Bud'ko, A. Kracher, R. J. McQueeney, R. W. McCallum, T. A. Lograsso, A. I. Goldman, and P. C. Canfield, Structural transition and anisotropic properties of single-crystalline SrFe_2As_2 , *Phys. Rev. B* **78**, 024516 (2008).
- [32] X.-G. Li, J.-M. Sheng, C.-K. Tian, Y.-Y. Wang, T.-L. Xia, L. Wang, F. Ye, W. Tian, J.-C. Wang, J.-J. Liu, H.-X. Zhang, W. Bao, and P. Cheng, Effects of vanadium doping on BaFe_2As_2 , *Europhys. Lett.* **122**, 67006 (2018).
- [33] G. M. Zhang, Y. H. Su, Z. Y. Lu, Z. Y. Weng, D. H. Lee, and T. Xiang, Universal linear-temperature dependence of static magnetic susceptibility in iron pnictides, *Europhys. Lett.* **86**, 37006 (2009).
- [34] See Supplemental Material at <http://link.aps.org/supplemental/10.1103/PhysRevB.107.224423> for details about representational analysis and fitting results of neutron diffraction data. The Supplemental Material also contains Refs. [15,21,23,43].
- [35] J. M. Allred, K. M. Taddei, D. E. Bugaris, M. J. Krogstad, S. H. Lapidus, D. Y. Chung, H. Claus, M. G. Kanatzidis, D. E. Brown, J. Kang, R. M. Fernandes, I. Eremin, S. Rosenkranz, O. Chmaissem, and R. Osborn, Double- Q spin-density wave in iron arsenide superconductors, *Nat. Phys.* **12**, 493 (2016).
- [36] W. Chen, X. Li, Z. Hu, Z. Hu, L. Yue, R. Sutarto, F. He, K. Iida, K. Kamazawa, W. Yu, X. Lin, and Y. Li, Spin-orbit phase behavior of $\text{Na}_2\text{Co}_2\text{TeO}_6$ at low temperatures, *Phys. Rev. B* **103**, L180404 (2021).
- [37] G. Cao, L. K. Rabenberg, C. M. Nunn, and T. E. Mallouk, Formation of quantum-size semiconductor particles in a layered metal phosphonate host lattice, *Chem. Mater.* **3**, 149 (1991).
- [38] C. Tian, F. Pan, L. Wang, D. Ye, J. Sheng, J. Wang, J. Liu, J. Huang, H. Zhang, D. Xu, J. Qin, L. Hao, Y. Xia, H. Li, X. Tong, L. Wu, J.-H. Chen, S. Jia, P. Cheng, J. Yang *et al.*, DyOCl : A rare-earth based two-dimensional van der Waals material with strong magnetic anisotropy, *Phys. Rev. B* **104**, 214410 (2021).
- [39] A. K. Nayak, J. E. Fischer, Y. Sun, B. Yan, J. Karel, A. C. Komarek, C. Shekhar, N. Kumar, W. Schnelle, J. Kubler, C. Felser, and S. S. P. Parkin, Large anomalous Hall effect driven by a nonvanishing Berry curvature in the noncolinear antiferromagnet Mn_3Ge , *Sci. Adv.* **2**, e1501870 (2016).
- [40] J.-X. Yin, S. S. Zhang, G. Chang, Q. Wang, S. S. Tsirkin, Z. Guguchia, B. Lian, H. Zhou, K. Jiang, I. Belopolski, N. Shumiya, D. Multer, M. Litskevich, T. A. Cochran, H. Lin, Z. Wang, T. Neupert, S. Jia, H. Lei, and M. Z. Hasan, Negative flat band magnetism in a spin-orbit-coupled correlated kagome magnet, *Nat. Phys.* **15**, 443 (2019).
- [41] M. Kang, L. Ye, S. Fang, J.-S. You, A. Levitan, M. Han, J. I. Facio, C. Jozwiak, A. Bostwick, E. Rotenberg, M. K. Chan,

- R. D. McDonald, D. Graf, K. Kaznatcheev, E. Vescovo, D. C. Bell, E. Kaxiras, J. van den Brink, M. Richter, M. Prasad Ghimire *et al.*, Dirac fermions and flat bands in the ideal kagome metal FeSn, *Nat. Mater.* **19**, 163 (2020).
- [42] M. Li, Q. Wang, G. Wang, Z. Yuan, W. Song, R. Lou, Z. Liu, Y. Huang, Z. Liu, H. Lei, Z. Yin, and S. Wang, Dirac cone, flat band and saddle point in kagome magnet YMn_6Sn_6 , *Nat. Commun.* **12**, 3129 (2021).
- [43] E. F. Bertaut, *Magnetism: A Treatise on Modern Theory and Materials*, edited by G. T. Rado and H. Suhl (Academic Press, New York, 1963), Vol. 3, p. 149.